

Carrier Localization and Cooling in Dye-Sensitized Nanocrystalline Titanium Dioxide

Gordon M. Turner, Matthew C. Beard, and Charles A. Schmuttenmaer*

Chemistry Department, Yale University, P.O. Box 208107, 225 Prospect Street,
New Haven, Connecticut 06520-8107

Received: March 27, 2002; In Final Form: July 22, 2002

The transient photoconductivity of dye-sensitized titanium dioxide has been measured using time-resolved terahertz spectroscopy, a noncontact electrical probe with sub-picosecond temporal resolution. The photoconductivity deviates strongly from Drude behavior and is explained by disorder-induced carrier localization and/or backscattering of the photogenerated carriers. In addition, the carriers are found to thermally equilibrate with the lattice in roughly 300 fs. Ramifications for understanding the function of DSSCs and electrical transport in disordered media are discussed.

Introduction

Porous networks of titanium dioxide (TiO_2) constitute the heart of the dye-sensitized solar cells (DSSCs) described by O'Regan and Grätzel in 1991.¹ DSSCs show promise as an efficient and low-cost alternative energy source, having demonstrated solar-to-electric energy conversion efficiencies of 10.4%.² The TiO_2 nanoparticles in a DSSC are sintered together to enable interparticle charge transport through the device, which is believed to proceed via a hopping mechanism over a distribution of barrier heights.^{3–6} Until now, the details of this transport have not been fully characterized. Here we present the first direct measurement of the microscopic carrier mobility immediately after charge injection in porous dye-sensitized nanocrystalline TiO_2 .

Time-resolved terahertz spectroscopy (TRTS) is a relatively new spectroscopic method that measures the frequency-dependent, complex-valued, far-infrared (0.2–2 THz, or 6–66 cm^{-1}) photoconductivity on subpicosecond time scales.^{7–11} It is the only technique capable of subpicosecond measurements in the far-infrared, and the fact that it is a noncontact electrical probe makes it ideally suited for the study of nanomaterials such as quantum dots and nanocrystals. TRTS is not sensitive to the adsorbed dye molecules of the DSSC because it measures only mobile charge carriers in the conduction band of the TiO_2 . DSSCs have been studied previously using ultrafast UV-pump/mid-infrared probe techniques that, like TRTS, are sensitive to charge carriers within the TiO_2 .^{12–14} Studies in the far-infrared region of the spectrum, however, provide far more information because carrier scattering rates are typically on the order of 1 to 10 THz.¹⁵ Time-resolved microwave conductivity (TRMC) measurements have also proven to be a very useful noncontact probe of porous TiO_2 , but with only nanosecond temporal resolution.¹⁶ We report the far-infrared conductivity of dye-sensitized porous TiO_2 films on a picosecond time scale and find that the Drude model, the simplest model of conductivity, is *not* an appropriate description. Models incorporating disorder-induced carrier localization or backscattering describe the data more accurately.

Experimental Methods

To extract the time-resolved frequency-dependent photoconductivity, the transmitted far-infrared electric field is measured as a function of temporal delay from a visible excitation pulse. Comparing this field to that transmitted by a nonphotoexcited sample yields the full frequency-dependent photoconductivity as described in ref 8. The sample is an air/photoexcited TiO_2 / TiO_2 /substrate dielectric stack, with a photoexcitation skin depth of 1.7 μm . The optical constants for nonphotoexcited TiO_2 and the quartz substrate must be measured separately.⁸ The nonphotoexcited TiO_2 film has negligible absorption and a nearly constant refractive index of 2.47. The refractive index is reduced significantly from the static permittivity of bulk anatase TiO_2 ($n \approx 7$) because our sample is an “effective” mesoporous TiO_2 /air film, with approximately 50% void space.

The samples consist of thin films (2.9 μm thick, measured with a DekTak 3030 profilometer) of Degussa P25 TiO_2 spun at 2000 rpm onto 1 mm thick fused silica etalon substrates (Precision Photonics).¹⁷ Degussa P25 consists of 25 nm particles that are 70% anatase and 30% rutile. The TiO_2 film is sensitized by soaking in an ethanol solution of $\text{Ru}(4,4'\text{-dicarboxy-2,2'-bipyridine})_2(\text{NCS})_2$ (Ru535). The dye sensitizer is photoexcited with a 100-fs duration 400-nm wavelength light pulse (130 μJ /pulse with an 8-mm diameter spot size). No more than 95% of the excitation beam is absorbed by the sample. This leads to about 50 photoexcited electrons per nanoparticle. Electrons are injected from the excited state of the dye molecule into the conduction band of the TiO_2 in less than 100 fs.^{12,18} While the photoexcitation wavelength of 400 nm is close to the band-edge of the TiO_2 , a 6-fold enhancement over the nonsensitized films is observed. Dye-sensitized Al_2O_3 , whose band-gap is too large to allow charge carriers to be injected, does not exhibit a TRTS signal. We have also measured the conductivity in networks of TiO_2 that have been sintered prior to dye sensitization, and see no qualitative differences in the extracted mobility or the carrier recombination dynamics. This is likely due to the fact that our measurement is sensitive to microscopic carrier mobilities that are unaffected by sintering. The samples were cooled to 77 Kelvin in a He-flow cryostat (Janis Scientific).

* Corresponding author's email: charles.schmuttenmaer@yale.edu.

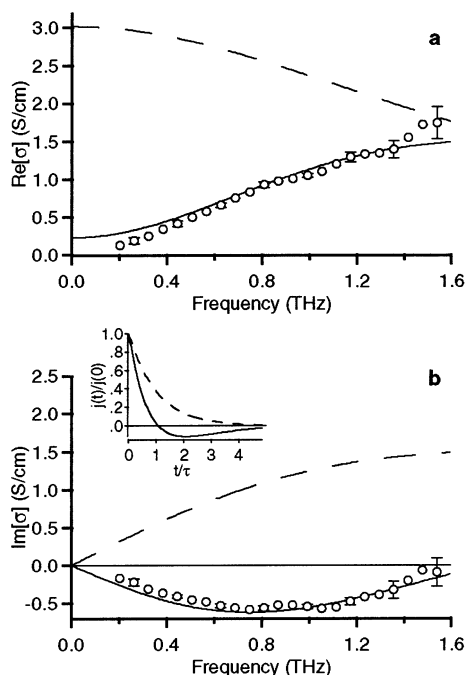


Figure 1. Experimentally determined real (a) and imaginary (b) parts of the conductivity at 77 K in unsintered TiO₂ sensitized with Ru535. Open circles are representative data taken 3 ps after photoexcitation, with the best fit of the Smith model shown as a solid line. The Drude conductivity is shown for comparison (dashed line). Parameters for the Smith model are $\omega_p = 20.7 \times 10^{12} \text{ s}^{-1}$, $\tau = 84 \text{ fs}$, and $c = -0.93$. The inset shows the current impulse response function $j(t)/j(0)$ for the Smith model with $c = -0.93$ (solid line) and Drude model (dashed line).

Results and Discussion

The Drude model describes the conductivity in metals and semiconductors quite well. The model, which describes a free electron gas subject to elastic scattering events with complete momentum randomization, dictates that the real component of the conductivity has its maximum at dc, and that the maximum of the imaginary component occurs at the radial frequency corresponding to the inverse scattering time τ of the carriers. There are many modifications of the Drude model that allow for a distribution of scattering times, but these basic features are common to most.^{7,19,20} The measured conductivity 3 ps after photoexcitation of dye-sensitized nanocrystalline TiO₂ is shown in Figure 1, and remains unchanged for delay times up to at least 1 ns. The deviation from Drude behavior (shown with the dashed lines) is striking: the real part of the conductivity increases with increasing frequency, and the imaginary part of the conductivity is *negative*. It is mathematically impossible for the Drude model and its simple variants to reproduce this behavior. We have verified that the photoconductivity in bulk single-crystal rutile TiO₂ (at 77 K) is in fact well described by the Drude model, yielding a scattering time of $\tau = 320 \text{ fs}$. This corresponds to a mobility $\mu = e\tau/m^*$ of $56 \text{ cm}^2 \text{ V}^{-1} \text{ s}^{-1}$ (using an electron effective mass of $m^* = 10 m_e$),²¹ which is comparable to published reports of $\mu = 10 \text{ cm}^2 \text{ V}^{-1} \text{ s}^{-1}$ at 100 K.²¹

Anomalous behavior of the low-frequency conductivity in disordered materials can be understood in terms of Anderson localization.^{22,23} Anderson's theory states that systems subject to disorder exhibit localization of their one-electron wave functions. Strongly disordered systems exhibit a distribution of trap states below the conduction band, resulting in thermally activated hopping transport behavior at low frequencies.²⁴ Mott

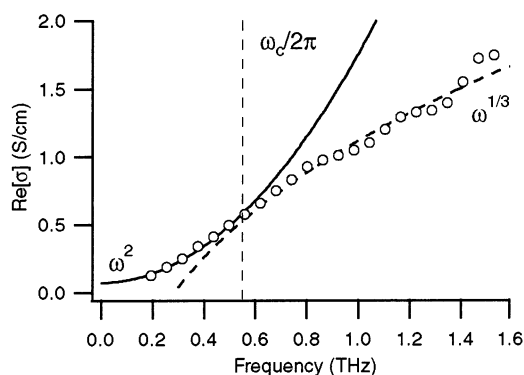


Figure 2. Fit of two functional forms to the real part of the conductivity to illustrate Anderson Localization. Data from 3 ps after photoexcitation is shown with open circles, ω^2 dependence is plotted as a solid line, and the $\omega^{1/3}$ dependence is plotted with a dashed line. A thin dashed vertical line is used to indicate the critical frequency $\omega_c/2\pi$. This frequency dependence is characteristic of a Fermi glass, or a system on the insulator side of the metal–insulator transition.²⁵

suggested that disorder suppresses the conductivity at long length scales (lower frequencies), leading to an enhancement at shorter wavelengths. The following frequency dependence of the real part of the conductivity is predicted

$$\text{Re}[\hat{\sigma}(\omega)] = \text{Re}[\hat{\sigma}(0)] + b\omega^s \quad (1)$$

where $\text{Re}[\hat{\sigma}(0)]$ is the dc conductivity, and b and s are constants.²⁵ Lee and co-workers find that $s = 2$ for $\omega < \omega_c$, and $s = 1/3$ for $\omega > \omega_c$ in conducting polymers on the insulator side of the metal–insulator transition. The critical frequency ω_c is related to the length scale of the disorder.²⁵ Our data clearly exhibit this dependence, as shown in Figure 2. The value of ω_c that describes our data best is $2\pi(0.55 \text{ THz})$, corresponding to a length scale of 5.4 to 17.1 nm depending on the effective mass of the electrons.^{26,27}

Smith proposed a classical modification to the Drude model that allows for a significant deviation from the general Drude features described above.^{28,29} The functional form of the model describes the complex conductivity $\hat{\sigma}(\omega)$ as

$$\hat{\sigma}(\omega) = \frac{\epsilon_0 \omega_p^2 \tau}{(1 - i\omega\tau)} \left[1 + \sum_{n=1}^{\infty} \frac{c_n}{(1 - i\omega\tau)^n} \right] \quad (2)$$

It consists of the basic Drude model, plus additional terms that account for the fraction of the carrier's initial velocity retained after experiencing the n th collision c_n . The free-space permittivity is ϵ_0 , τ is the carrier collision time, $\omega = 2\pi\nu$ is the radial frequency, and the plasma frequency is given by $\omega_p^2 = Ne^2/(\epsilon_0 m^*)$, where N is the carrier density and m^* is the carrier effective mass. As discussed in ref 29, only the first term in the summation is retained, and c_1 is denoted c . When $c = 0$, the standard Drude model is obtained. When $c = -1$, the real part of the conductivity is 0 at dc and the imaginary part of the conductivity is negative at low frequencies as seen in Figure 1. This is interpreted as conductivity dominated by backscattering.²⁹ Smith has applied this model to the optical conductivity of liquid Hg and Te, as well as the quasicrystal Al_{63.5}Cu_{24.5}-Fe₁₂, all of which are systems that can be described as poor conductors, or materials near the metal–insulator transition.²⁹ A time-domain picture of the conductivity is provided by the current impulse response function. When $c = -1$ the response function becomes negative at $t/\tau = 1$ (see inset of Figure 1), resulting in zero net current displacement or, equivalently, zero

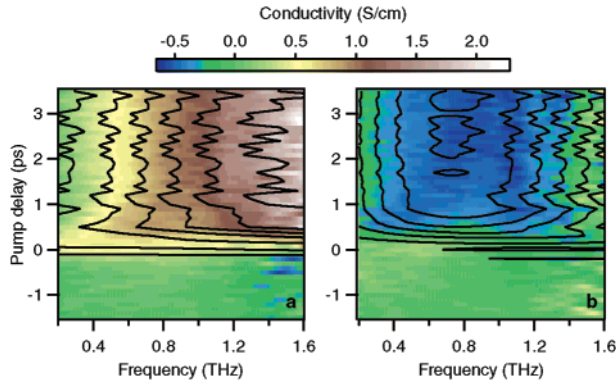


Figure 3. Real (a) and imaginary (b) parts of the frequency-dependent conductivity in Ru535/TiO₂ as a function of delay from the pump pulse arrival time. The contour lines are based on a global fit that contains an outer fitting loop in which the carrier density is parametrized as a function of time by a Heaviside step function convoluted with a Gaussian. An inner loop of the fit optimizes the Smith model to the data at a given time after photoexcitation using a fixed value for the carrier density as determined in the outer loop. The extracted parameters are a Gaussian full-width half-maximum of 215 fs, and a plasma frequency of $\omega_p = 19.8 \times 10^{12} \text{ s}^{-1}$ (see Figure 5).

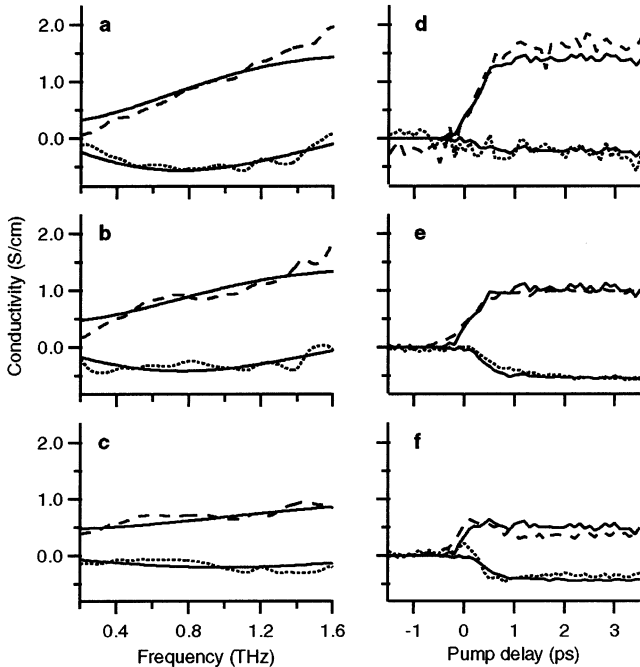


Figure 4. Real (dashed lines) and imaginary (dotted lines) components of the conductivity from the 2D grid of Figure 3, with results from the Smith model (solid lines). Parts a, b, and c show the frequency-dependent conductivity at 2.0, 0.5, and 0.2 ps after photoexcitation, respectively. Parts d, e, and f display the time-dependent conductivity at selected frequencies of 1.4, 0.9, and 0.4 THz, respectively.

dc conductivity. Values of c near -1 result in small fractional current displacements and small (but nonzero) dc conductivity. Smith's model best represents our data when $c \approx -0.9$, as indicated by the best fit to the data shown in Figure 1.

Two-dimensional grids of the complex-valued photoconductivity as a function of time after photoexcitation are shown in Figure 3. Overlaid are contour plots resulting from a global two-dimensional fit of Smith's model to the data (see caption for details). Cuts through selected time and frequency values are shown in Figure 4 to illustrate the high quality of the fit. Smith's model accurately describes the data at all pump–probe delay times. Plots of the parameters τ and c as a function of pump

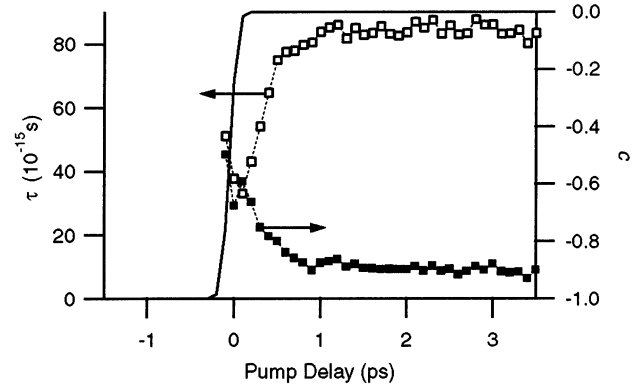


Figure 5. Plot of the carrier scattering time τ (open squares) and c (solid squares) as a function of pump delay time based on global fit described in Figure 3. The solid line indicates the onset of photoconductivity.

delay time are shown in Figure 5. As the initially hot carriers cool to the conduction band edge by emission of LO phonons, the time between collisions increases exponentially from 32 fs to a value of 84 fs with a time constant of 190 fs. The time-dependence of the c parameter is similar, starting at a value of -0.65 and decaying on a 330 fs time scale to a value of -0.9 . This indicates that the conductivity is initially more Drude-like, and then evolves into a conduction dominated by backscattering ($c \approx -0.9$) as the carriers equilibrate with the lattice, becoming more susceptible to scattering off of grain boundaries and nanoparticle surfaces.

The carrier density N is calculated to be $1.2 \times 10^{18} \text{ cm}^{-3}$ (using the anatase effective mass²⁶ of $10m_e$). Assuming the films consist of 50% void space leads to an average density of about 20 electrons per particle. This is a factor of 2.5 less than the carrier density estimated from the input photon flux, but could be due to several factors such as reflectivity losses that were not accounted for, or electrons that reside in deep traps and are not detected by the THz probe pulse. The Drude model, and Smith's modification, assumes that the electrons are independent. This assumption is valid when carriers are separated on average by an amount greater than their screened Coulombic interaction length, $l_c = e^2/4\pi\epsilon_0\epsilon_k k_B T$, which is 2.2 nm for rutile. This corresponds to an upper limit for the carrier density of $2.3 \times 10^{19} \text{ cm}^{-3}$ at 77 K, or 188 electrons per 25 nm diameter particle. This indicates that the densities used in these experiments will not affect our results other than decreasing the magnitude of the conductivity.

Once the carriers have cooled to the conduction band edge, their mean free path $l = v_{th}\tau$ can be calculated based on their thermal velocity $v_{th} = \sqrt{3k_B T/m^*}$.¹⁵ In bulk rutile TiO₂, the mean free path calculated from our measurement of the conductivity is about 6 nm (using an electron effective mass of $10m_e$).²¹ Confining the carriers to a spherical nanoparticle of 25 nm diameter results in an effective mean free path of $l_{eff} \leq 4.0 \text{ nm}$ according to Mattheissen's rule³⁰

$$\frac{1}{l_{eff}} \geq \frac{1}{\text{radius}} + \frac{1}{l_{bulk}} \quad (3)$$

We measure a mean free path in the nanoparticles of 1.6 nm ($\tau = 84 \text{ fs}$ and the anatase effective mass is $m^* = 10 m_e$),²⁶ in agreement with the inequality of Mattheissen's rule. This indicates that the reduced mobility (and mean free path) in the P25 nanoparticles can be explained by the presence of additional

scattering processes, in agreement with the models of disorder-induced localization and carrier backscattering already presented.

We calculate the ac mobility, based on the scattering time and effective mass, to be $\mu = 15 \text{ cm}^2 \text{ V}^{-1} \text{ s}^{-1}$. According to the Smith model with a c parameter of -0.9 , the dc mobility will be a factor of 10 less than the ac mobility, or $1.5 \text{ cm}^2 \text{ V}^{-1} \text{ s}^{-1}$. This is orders of magnitude greater than reported drift mobilities of electrons in DSSCs,^{31,32} but is closer to the $0.09 \text{ cm}^2 \text{ V}^{-1} \text{ s}^{-1}$ reported at GHz frequencies from TRMC measurements.¹⁶ This discrepancy in the dc mobility is likely due to the fact that our lowest frequency data is at 200 GHz, and we extrapolate to dc. While the ac mobility is reduced from what is observed in bulk TiO_2 , the intraparticle mobility is very high compared to the low dc mobilities often reported. The idea of highly mobile electrons within TiO_2 nanoparticles is in stark contrast to theoretical models based on low experimental drift mobilities, which describe electrons as trapped at the surface of the nanoparticle and are only occasionally mobile as they hop from trap to trap.^{3,4}

Conclusions

These TRTS results demonstrate that the carriers within TiO_2 nanoparticles deviate from their bulk Drude-like behavior. However, at short length scales the carriers are still quite mobile, with longer range transport hindered by disorder. A similar conclusion was postulated based on TRMC measurements of several different TiO_2 morphologies.¹⁶ We have provided an unprecedented level of detail about the microscopic nature of charge transport in nanocrystalline TiO_2 films. By measuring the frequency-dependent complex conductivity on a sub-picosecond time scale, we have shown that carrier cooling within the conduction band occurs in about 300 fs. These observations are consistent with the present understanding of dc transport in actual DSSC assemblies, and provide new insight into the nature of the conduction mechanism. Present models describe a power-law dc transport behavior in DSSCs arising from trapping/detrapping with a distribution of barrier heights.^{3,4} Activated transport, as incorporated into these continuous-time random walk (CTRW) models,^{3,4} is also implicit in the Anderson description of a disordered material on the insulator side of the metal–insulator transition, and as such is *not* contradicted by our measurements. The microscopic interpretation of transport processes as arising from trapping/detrapping *within* nanoparticles, however, is inconsistent with our new observations. It is now clear that electrons within nanoparticles are quite mobile, yet their bulk transport is hindered by disorder.

Acknowledgment. Partial support from the Sloan Foundation and from the National Science Foundation CAREER award program (CHE-9703432) is gratefully acknowledged. G.M.T. acknowledges support from Sigma Xi Grants in Aid of Research.

References and Notes

- (1) O'Regan, B.; Gratzel, M. *Nature* **1991**, *353*, 737–740.
- (2) Nazeeruddin, M. K.; Pechy, P.; Renouard, T.; Zakeeruddin, S. M.; Humphry-Baker, R.; Comte, P.; Liska, P.; Cevey, L.; Costa, E.; Shklover, V.; Spiccia, L.; Deacon, G. B.; Bignozzi, C. A.; Gratzel, M. *J. Am. Chem. Soc.* **2001**, *123*, 1613–1624.
- (3) Nelson, J.; Haque, S. A.; Klug, D. R.; Durrant, J. R. *Phys. Rev. B* **2001**, *63*, 5321.
- (4) Nelson, J. *Phys. Rev. B* **1999**, *59*, 15374–15380.
- (5) Hagfeldt, A.; Gratzel, M. *Acc. Chem. Res.* **2000**, *33*, 269–277.
- (6) Gratzel, M. *Nature* **2001**, *414*, 338–344.
- (7) Beard, M. C.; Turner, G. M.; Schmittenmaer, C. A. *Phys. Rev. B* **2000**, *62*, 15764–15777.
- (8) Beard, M. C.; Turner, G. M.; Schmittenmaer, C. A. *J. Appl. Phys.* **2001**, *90*, 5915–5923.
- (9) Jepsen, P. U.; Schairer, W.; Libon, I. H.; Lemmer, U.; Hecker, N. E.; Birkholz, M.; Lips, K.; Schall, M. *Appl. Phys. Lett.* **2001**, *79*, 1291–1293.
- (10) Averitt, R. D.; Rodriguez, G.; Lobad, A. I.; Siders, J. L. W.; Trugman, S. A.; Taylor, A. J. *Phys. Rev. B* **2001**, *63*, 0502+.
- (11) Huber, R.; Tauser, F.; Brodschelm, A.; Bichler, M.; Abstreiter, G.; Leitenstorfer, A. *Nature* **2001**, *414*, 286–289.
- (12) Ellingson, R. J.; Asbury, J. B.; Ferrere, S.; Ghosh, H. N.; Sprague, J. R.; Lian, T. Q.; Nozik, A. J. *J. Phys. Chem. B* **1998**, *102*, 6455–6458.
- (13) Heimer, T. A.; Heilweil, E. J. *J. Phys. Chem. B* **1997**, *101*, 10990–10993.
- (14) Ghosh, H. N.; Asbury, J. B.; Lian, T. Q. *J. Phys. Chem. B* **1998**, *102*, 6482–6486.
- (15) Ashcroft, N. W.; Mermin, N. D. *Solid State Physics*; Saunders College Publishing: New York, 1976.
- (16) Savenije, T. J.; de Haas, M. P.; Warman, J. M. Z. *Phys. Chem. – Int. J. Res. Phys. Chem. Chem. Phys.* **1999**, *212*, 201–206.
- (17) Nazeeruddin, M. K.; Kay, A.; Rodicio, I.; Humphrybaker, R.; Muller, E.; Liska, P.; Vlachopoulos, N.; Gratzel, M. *J. Am. Chem. Soc.* **1993**, *115*, 6382–6390.
- (18) Asbury, J. B.; Ellingson, R. J.; Ghosh, H. N.; Ferrere, S.; Nozik, A. J.; Lian, T. Q. *J. Phys. Chem. B* **1999**, *103*, 3110–3119.
- (19) Jeon, T. I.; Grischkowsky, D. *Appl. Phys. Lett.* **1998**, *72*, 3032–3034.
- (20) Jeon, T. I.; Grischkowsky, D. *Phys. Rev. Lett.* **1997**, *78*, 1106–1109.
- (21) Goodenough, J. B.; Hamnett, A. *Semiconductors, Group III: Crystal and Solid State Physics*; Springer-Verlag: Berlin, 1984; Vol. 17g.
- (22) Mott, N. F. *Metal–Insulator Transitions in Doped Semiconductors: A survey. Localization and Interaction in Disordered Metals and Doped Semiconductors*. University of St. Andrews, St. Andrews, Fife, Scotland, U.K., 1986.
- (23) Lee, P. A.; Ramakrishnan, T. V. *Rev. Mod. Phys.* **1985**, *57*, 287–337.
- (24) Mott, N. F. *Philos. Mag.* **1969**, *19*, 835–852.
- (25) Lee, K. H.; Menon, R.; Yoon, C. O.; Heeger, A. J. *Phys. Rev. B* **1995**, *52*, 4779–4787.
- (26) Enright, B.; Fitzmaurice, D. *J. Phys. Chem.* **1996**, *100*, 1027–1035.
- (27) Tang, H.; Prasad, K.; Sanjines, R.; Schmid, P. E.; Levy, F. J. *Appl. Phys.* **1994**, *75*, 2042–2047.
- (28) Smith, N. V. *Phys. Lett. A* **1968**, *26*, 126.
- (29) Smith, N. V. *Phys. Rev. B* **2001**, *64*, 5106.
- (30) Mulvaney, P. *Langmuir* **1996**, *12*, 788–800.
- (31) Van der Zanden, B.; Goossens, A. J. *Phys. Chem. B* **2000**, *104*, 7171–7178.
- (32) Dittrich, T. *Phys. Status Solidi A* **2000**, *182*, 447–455.